Biosensors and Bioelectronics 196 (2022) 113696

Contents lists available at ScienceDirect

Biosensors and Bioelectronics

journal homepage: www.elsevier.com/locate/bios

A machine learning-enhanced biosensor for mercury detection based on an hydrophobin chimera

Anna Pennacchio [a], Fabio Giampaolo [b], Francesco Piccialli [b,*], Salvatore Cuomo [b], Eugenio Notomista [c], Michele Spinelli [a], Angela Amoresano [a], Alessandra Piscitelli [a,**], Paola Giardina [a]

[a] Department of Chemical Sciences, University of Naples Federico II, Italy
[b] Department of Mathematics and Applications "R. Caccioppoli", University of Naples Federico II, Italy
[c] Department of Biology, University of Naples Federico II, Italy

ARTICLE INFO

Keywords:
Heavy metals
Artificial intelligence
Sea water
Histidine-rich peptide
Fluorescence quenching
Amyloid autofluorescence

ABSTRACT

Marine waters are becoming contaminated by diverse pollutants at a fast rate, and detection of these water pollutants has become a major concern in recent years. Among these, mercury is considered the most toxic element for human health. At present, despite the commonly used methods for its detection are accurate, they often require sophisticated equipments, have relatively high costs, are demanding and time-consuming.

Herein a novel solution to detect mercury (II) pollution in sea water is proposed, and an easy and portable detection method has been developed. Indeed, a hydrophobin based chimera able to both adhere to polystyrene multiwell plates and bind mercury (II) with a consequent fluorescent decrease was designed. The chimera was the recognition element in a fluorescence-based biosensor able to detect mercury (II) in the nM range. Indeed, this biosensor specifically measure Hg^{2+} concentration also in the presence of other metals, reaching a limit of detection of 0.4 nM in tap water and 0.3 nM in sea water. Moreover, the developed biosensor was coupled to machine learning methodologies with the big advantage of predicting mercury concentration levels without the use of classical reader devices, thus allowing *in situ* monitoring of sea pollution by non-skilled personnel.

1. Introduction

Heavy metals are universally toxic to biological organisms when present in excess and are the source of substantial environmental and health problems (De Silva et al., 2002). They are difficult to remove from the environment and, unlike many other pollutants, cannot be chemically or biologically degraded, therefore, constitute a global environmental hazard (Vardhan et al., 2019). Among them, mercury and its compounds are regarded as "priority hazardous substances" by the Agency for Toxic Substances and Disease Registry (ATSDR) because of its toxicity, mobility, long residence time, and biomagnification in food chains (Mahurpawar, 2015). For examples, Hg^{2+} is highly toxic even at low levels, and in humans it can affect liver, kidneys and cardiovascular, gastrointestinal and neurological systems (Jyothi et al., 2020). Anthropogenic activities such as mining, incineration, agriculture, discharge of municipal and industrial wastewater, shipping movements, and combustion of motor fuels are the major sources of mercury pollution (Chopra et al., 2009; Nour and El-Sorgy, 2020).

In recent years, the pollution of the aquatic environment with heavy metals has become a global problem. Heavy metals are one of the most common pollutants which have severely deteriorated the aquatic ecosystems due to their toxicity, abundance, persistence, and subsequent bio-accumulation (Ali et al., 2013).

To cope with the serious threat of mercury contamination to the ecosystem and human health, many instrumental methods have been developed to detect aqueous Hg^{2+} and to assess its risks (Huang et al., 2019), such as cold vapour integrated quartz crystal microbalance (CV-QCM) (Kabir et al., 2019), gas chromatography-triple quadrupole

* Corresponding author.
** Corresponding author.
E-mail addresses: anna.pennacchio@unina.it (A. Pennacchio), fabio.giampaolo@unina.it (F. Giampaolo), francesco.piccialli@unina.it (F. Piccialli), salvatore.cuomo@unina.it (S. Cuomo), notomist@unina.it (E. Notomista), mic.spinelli87@gmail.com (M. Spinelli), angela.amoresano@unina.it (A. Amoresano), apiscite@unina.it (A. Piscitelli), giardina@unina.it (P. Giardina).

https://doi.org/10.1016/j.bios.2021.113696
Received 19 July 2021; Received in revised form 23 September 2021; Accepted 6 October 2021
Available online 9 October 2021

mass spectrometry (GC-MS/MS) (Li et al., 2019), electrochemical sensors (Shah et al., 2019), mercury analyzers (de la Calle et al., 2019), fluorescence, colorimetric (Gu et al., 2019), and atomic absorption spectroscopy (Saleh et al., 2020). Although the accuracy of these methods is high, they often require sophisticated laboratory based equipment and have relatively high costs. The process is demanding and time-consuming, which cannot meet the needs of high-efficiency and low-cost in actual monitoring. Thus, the development of simple, cost-effective, rapid, and portable sensing devices is still needed (Justino et al., 2017). In this context, biosensors, with their reduced cost and quick measurement, meet all these requirements and are, indeed, replacing the other demanding analytical techniques (Liu et al., 2019). Portable lab-on-hardware is a research field with broad applications in organic classification, disease diagnosis, environmental surveillance, and bioresearch. Since smartphones (SP) are lightweight and widely available, they are particularly suited for on-site analysis. As regards Image Acquisition, many mobile sensors have been developed for SP using attached 3D printed optical interface with physical detection instruments (Vashist and Luong, 2019).

Among sensing molecules, metal binding peptides are particularly suitable for the development of fluorescent probes, thanks to the combination of several benefits, such as structural complexity and flexibility allowing the achievement of easy tuneable properties as well as the desired specificity. In previous works, inspired by the variety of functions of histidine-rich glycoproteins (HRGs), a peptide fluorescent probe was designed containing the repeated sequence of human HRG (HPHGH) plus a dansyl group and a tryptophan residue at the two ends. This peptide, named dH3w (dansyl-HPHGHW-NH_2) (Donadio et al., 2016) turned out to be a very sensitive probe for the detection of Hg^{2+} for environmental monitoring purposes (Siepi et al., 2018). In view of the development of biosensors, proteins immobilization on a solid support is crucial, since it can highly affect the handling, the functionality and consequently the performance of the device (Faccio, 2018). Opposed to chemical crosslinkers, protein engineering through fusion of proteins at the gene level offers intriguing approaches to the functionalization of surfaces with well-oriented proteins (Koji et al., 2006; Choi et al., 2011). In this context, fusion of adhesive proteins, like the fungal self-assembling proteins named hydrophobins with specific sensing proteins has already demonstrated very good potential (Hennig et al., 2016). In particular, the class I hydrophobin Vmh2 from the fungus *Pleurotus ostreatus*, a surface-active, self-assembling, adhesive protein, able to adhere on many conventional and 2D surfaces (De Stefano et al., 2009; Gravagnuolo et al., 2015; Kaur et al., 2017), is a case in point (Piscitelli et al., 2017a, 2017b; Sorrentino et al., 2019, 2020; Puopolo et al., 2021).

In this work we designed a new Vmh2-based chimera with the aim to easily immobilize the H3w peptide onto a multiwell plate and develop two alternative methods for measuring Hg^{2+} by fluorescence analysis. The first method exploits the near-UV fluorescence of the tryptophan residues in H3w and a conventional multiwell plate reader. The second method exploits the so-called blue-green autofluorescence of amyloid fibrils – a relatively new and not completely understood phenomenon (Sirangelo et al., 2018) – and novel predictive algorithms to classify concentration levels, allowing Hg^{2+} detection without the use of classical reader devices.

Indeed, we propose a strategy based on Machine Learning (ML) to automatically recognize wells of a multiwell to predict the fluorescence intensity values connected to the concentration of heavy metals without the need for a specific reader. Our pipeline is articulated in two stages, the first of whom focuses on image processing and feature extraction: on acquired images, a combination of cropping (Hatiboruah et al., 2020), channel selection, and average of intensities (Kim et al., 2021) are well-known pre-processing methodologies. A task of particular importance is the Region Of Interest (ROI) identification (Berg et al., 2015) for correctly detecting the positions of the wells on a well-plate. About the automatic features extraction related to information in wells, we consider the techniques might include Region Adjacency Graph (RAG) segmentation (Akmal et al., 2019), edge detection (Canny, 1986) and Hough circle detection algorithm (Yuen et al., 1990). Finally, for image matching, inspiring algorithms can be found as in (Lowe, 2004). The idea behind this task is to map precisely the position of wells on a reference image since the well plate is standardized.

The second stage of the pipeline combines three machine learning algorithms (Multi-layer Perceptron, Random Forest, and XGBoost) for classification and prediction tasks. As regards these methodologies in processing data from biosensors, there are increasing interest in these algorithms (Cui et al., 2020), as, for example, support vector machine (SVM), Naive Bayes (NB), decision tree.

(DT), gradient-boosted trees (GBT), random forest (RF), and artificial neural network (ANN) like Multilayer perceptron (MLP) (James et al., 2013).

The learning procedures of our pipeline were trained to recognize the fluorescence levels of a water containing Hg^{2+}. We designed our architecture to identify wells in two different light environments: (*i*) portable UV light, (*ii*) diffusive fixed UV lights. So ultimately, our goal was the development of a portable and easy to use device to detect Hg^{2+} also in polluted seawater useable *in situ* and by non-specialized personnel.

2. Materials and methods

2.1. Materials

Reagents were purchased from Sigma-Aldrich (Saint Louis, Missouri, USA). Expression vectors and yeast strains were purchased from Biogrammatics, Ltd (Las Palmas Dr, Carlsbad, CA, USA). DNA restriction and modifying enzymes were supplied by Promega (Madison, WI, USA). The fusion protein encoding gene was synthesized by Thermo Fischer Scientific (Waltham, Massachusetts, USA). Culture media were bought from BD Difco (Becton Drive, Franklin Lakes, NJUSA). Mercury chloride, zinc sulfate, copper nitrate and cobalt nitrate were purchased from Sigma.

Concentrated nitric (UpA) and hydrochloric (UpA) acids, and certified stock standard solutions were purchased from Romil.

2.2. Vector construction

A synthetic gene encoding for Vmh2 from *P. ostreatus* in frame with a suitable linker, the fluorescent peptide His-Pro-His-Gly-His-Trp (H3w) (Donadio et al., 2016), the thrombin cleavage site and the GFP from *Aequorea victoria* was designed (1008 bp) and optimized according to *Pichia pastoris* codon usage. The gene product was restricted with *BsaI* and ligated into the corresponding site of the pJGG_αkR vector in-frame with the α-factor (signal peptide) under the control of the constitutive GAP promoter, yielding the recombinant plasmid pJGG_Vmh2-H3w-GFP. The recombinant plasmid was linearized by *BsiWI* and transformed into *P. pastoris* BG-10.

2.3. Transformation of P. pastoris and screening of the clones

P. pastoris cells were collected from a solid culture and grown in 50 mL of YPD medium (10gL^{-1}yeast extract, 20 g L^{-1} bacto tryptone, 20 g L^{-1} glucose) at 28 °C on a rotary shaker (150 rpm) over night. The overnight culture was diluted 1:5000 in fresh medium and grown overnight up to 1.3–1.5 OD_{600}. Next, the cells were sedimented by centrifugation at 2000 rpm at 4 °C for 5 min, resuspended in YPD, 0.02 M Hepes, 0.04 M DTT, and shaken at 30 °C for 25 min at 100 rpm. Then the cell suspension was diluted 1:10 with cold H_2O and the cellular pellet washed with cold H_2O, and cold 1 M sorbitol. The cell pellet was then resuspendend in 1 M sorbitol and mixed with the linearized transforming DNA plasmid (up to 0.5 μg).

P. pastoris transformation was performed by electroporation with a

Bio-RadMicro-Pulser apparatus (BioRad, Hercules, California, USA), as specified by the manufacturer. Immediately afterwards, 1 mL of Recovery Media (1:1 YPD: sorbitol) was added to the electroporation cuvette and the whole content was transferred to a sterile tube. The tube was then incubated at 28 °C for 3 h under shaking conditions. The cell suspension was spread on YPD plates containing 900 μg mL^{-1} of G418 and incubated for 3–7 days at 28 °C until colony formation. The colonies were collected, inoculated in Minimal Dextrose Medium (MD) (13 g L^{-1} Yeast Nitrogen Base with ammonium sulfate w/o amminoacids, 4 × 10^{-4} g L^{-1} biotin, 20 g L^{-1} glucose), and grown at 28 °C on a rotary shaker (250 rpm). Aliquots were daily withdrawn and assayed for cell density and for GFP fluorescence emission using the Synergy H4 (Biotek Instruments, Winooski, Vermont, USA) acquiring data through top-reading mode. The excitation wavelength was fixed at 450 nm and emission spectra were recorded between 460 and 560 nm. The emission spectra were then corrected by subtracting the blank (the supernatant of the wild-type *P. pastoris* strain).

2.4. Expression and purification of the fusion protein Vmh2-H3w-GFP

Pre-inoculum preparation of the recombinant selected clone was performed at 28 °C overnight in MD. The pre-inoculum was diluted 1:100 in the same medium. After 8 days the cells were removed by centrifuging for 20 min at 7000 rpm at 4 °C. The supernatant was recovered, concentrated and dialyzed towards 50 mM Tris-HCl buffer, pH 8.0, using Centricon Centrifugal Filter Units withUltracel YM-10 membrane (Merck, Darmstadt, Germany). The protein concentration was determined using the Bradford method (BioRad) according to the manufacturer's instructions and using BSA as the standard.

2.5. Vmh2-H3w-GFP immobilization into multi-well plates

100 μl of Vmh2-H3w-GFP at different concentration (from 0.005 to 0.1 mg ml L^{-1}) were deposited into polystyrene multi-well plates (96 wells). Controls were performed immobilizing 100 μl of the supernatant of the wild-type *P. pastoris* strain at the same protein concentration. The fusion protein was incubated into the polystyrene well at 28 °C overnight. After incubation, the residual liquid was removed, then the wells were washed threefold with 50 mM Tris HCl buffer, pH 8.0 to eliminate any unbound proteins, and the intensity of fluorescence of the protein was measured both in the washes and into the wells. The excitation wavelength was fixed at 450 nm and emission spectra were recorded between 460 and 560 nm, with maximum of emission at 495 nm. To assess the yield in terms of protein amount, the immobilized content was calculated as the difference between the quantity used for the immobilization and that measured in the residual liquid and in the washings.

To obtain Vmh2-H3w and separate it from GFP, 100 μL of thrombin (6 U) were added (Pennacchio et al., 2018) to the functionalized wells and incubated at 37 °C for 30 min. The supernatant was recovered and assayed for GFP (excitation wavelength at 450 nm and maximum of emission at 495 nm). In order to evaluate that the peptide was immobilized on the multiwell, emission spectra were recorded in the range 350–600 mm after excitation at 295 nm and the maximum of emission at 360 nm was used. The slit size for excitation and emission wavelengths was 10 nm.

To evaluate the stability of the immobilized Vmh2-peptide, the fluorescence intensity at 360 nm was measured every day in different wells of a plate stored dry at room temperature.

Fibril autofluorescence was evaluated recording emission spectra in the range 360–600 mm after excitation at 345 nm depositing 100 μl of protein samples (Vmh2-H3w, Vmh2) at 0.005 mg ml L^{-1}.

2.6. Metal assay

Fluorescence intensity of Vmh2-H3w in the presence of different metals (Hg^{2+}, Cu^{2+}, Zn^{2+}, Ni^{2+} Co^{2+}, and Mg^{2+}) was assayed at room temperature in sodium-phosphate buffer at pH 7 at increasing metal concentrations (from 1 nM to 1 mM) for 15 min. Then, after excitation at 295 nm the fluorescence intensity at 360 nm was measured.

The fluorescence emission intensity of immobilized Vmh2-H3w was also recorded in the presence of mixtures of Hg^{2+} and different metal ions in 50 mM sodium phosphate, pH 7.0.

In order to reduce Cu^{2+} to Cu^{+} thus avoiding its binding to the peptide and determine only the Hg^{2+} concentration, ascorbic acid (50 nM, 100 μM, 1 mM) was added to the sample and incubated at room temperature for 10 min. Then 100 μL of the sample were added to the functionalized well and analysed as above mentioned.

The detection limit (LOD) for Hg^{2+} was calculated by performing a fluorescence titration. The emission intensity of Vmh2-H3w without metal ions was measured ten times, and the standard deviation of the blank measurements was determined. Hence the fluorescence was measured by increasing the Hg^{2+} concentration up to 1 mM. In our study, a logarithmic dependence was observed, therefore LOD was calculated according to (Hao et al., 2018) using the equation reported below, where a is the intercept, b the slope, s_a, s_b, s_x and s_y the deviation of the intercept, the slope, the concentration and the response signal, respectively. When y is placed by the blank signal y_0; s_y is changed to s_{y0}.

$$x_D = ts_x = \frac{t}{b} e^{\frac{y_0 - a}{b}} \left[s_{y0}^2 + s_a^2 + \left(\frac{y_0 - a}{b} \right)^2 s_b^2 \right]^{\frac{1}{2}}$$

The confidence factor t = 3 is chosen corresponding to the probability of making the confidence level of 95%. In our analysis, the analyte concentration (x) is the Hg^{2+} concentration; the response signal (y) is the value of fluorescence intensity at 360 nm.

A sensor calibration curve for sea water was obtained by spiking different concentrations of Hg^{2+} in the range of 1 nM to 1 mM in sea water. Sea water samples were collected at Paestum, Salerno (Italy). A sensor calibration curve was similarly obtained in tap water.

To evaluate the reusability of the functionalized plate, 200 μL of 10 mM EDTA were added to the multiwell and incubated at different time (10–120 min) at room temperature (25 °C).

2.7. Mass spectrometry analyses

Standard solutions containing Cu^{2+} and Zn^{2+} were prepared in 3% Nitric Acid at five different concentrations, (0, 1, 10, 50 and 100 μg L^{-1}). A separate set of standard solution was prepared for Hg^{2+} in 2% Nitric Acid and 1% Hydrochloric Acid, (0, 1, 10, 20 and 50 μg L^{-1}).

Samples were diluted in 3% HNO_3 for the analysis of Cu^{2+} and Zn^{2+} and in 2 %HNO_3 and 1% HCl for the analysis of Hg^{2+}. Metal concentrations have been measured with three replicates.

Measurements have been performed with an Agilent 7700 ICP-MS instrument (Agilent Technologies) equipped with a frequency-matching radio frequency (RF) generator and 3rd generation Octapole Reaction System (ORS3) operating with helium gas in ORF. The following parameters were used: RF power: 1550 W, plasma gas flow: 14 L min^{-1}; carrier gas flow: 0.99 L min^{-1}; He gas flow: 4.3 mL min^{-1}^{103}Rh was used as an internal standard (final concentration: 50 μg L^{-1}).

2.8. Data pre-processing

In order to develop an automatic strategy based on ML methodologies to recognize fluorescence levels of samples, we collected a dataset composed of more than 700 mobile shots of a 96-well microplate (or multiwell) with standard dimensions (127.71 mm × 85.43 mm). Each microplate has 12 columns (1–12) and 8 rows (A-H). Photos were taken using smartphones, adopting their automatic exposure setting in the following light configurations (Fig. 1a):

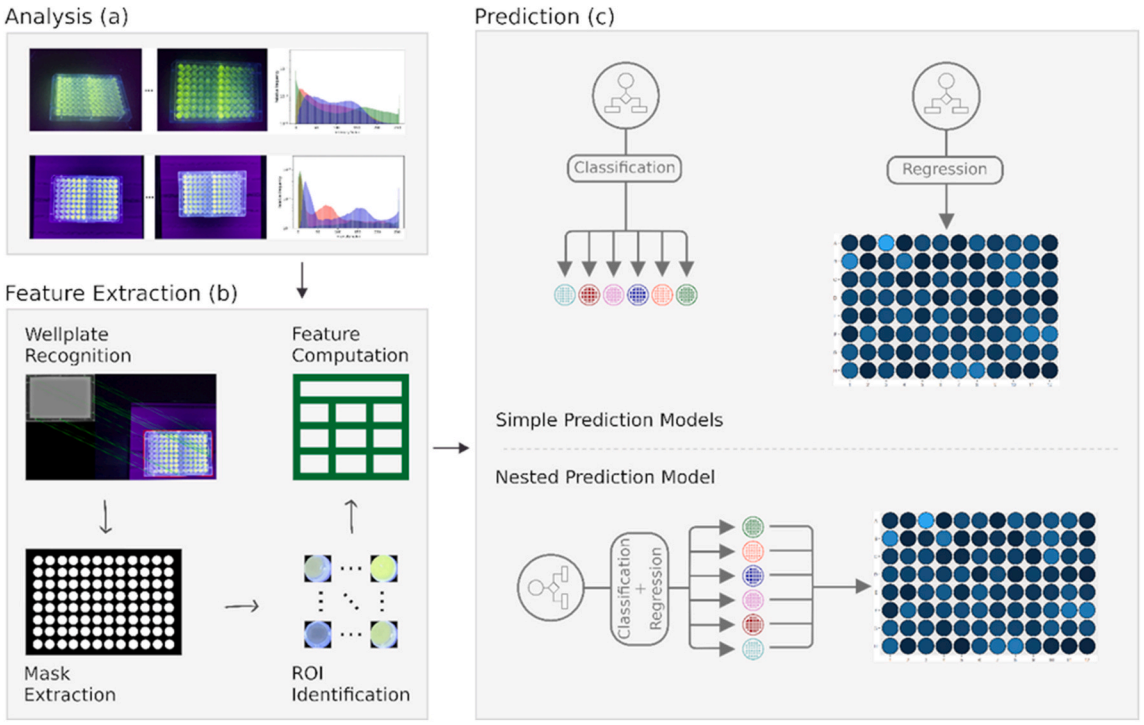

Fig. 1. Schematic representation of the workflow and its phases. (a) Images collected in different light conditions (UV, UVp) are preliminary analysed to find the most representative color space. **(b)** A reference image is chosen and the region of the well plate on the photo is identified. For each image a mask is then generated and images containing each of the wells, i.e. the ROIs, are extracted. From these, numerical features related to each sample are computed and stored in a tabular shape. **(c)** The obtained dataset is fed to ML models to provide classification and regression about concentration classes and real fluorescence values, respectively. Moreover, to enhance the performances on the regression task, a nested model is designed. (For interpretation of the references to colour in this figure legend, the reader is referred to the Web version of this article.)

- portable UVc (PUVc), in which the well plates are directly illuminated by a portable UVc emitting lamp placed in the operator's hands;
- UVc, with a steady UV light coming from behind a fixed well plate, in a dark room.

During the image processing phase, a major issue is identification of the structure of the well plate (which is transparent). It is a common practice to project images onto different colour maps to gain new insights. In our case, we found that the CIELAB colour space was the most useful, in particular the b layer since it brings out the colour scale from blue to yellow, and was able to well intercept the blue-scale reflection generated by the plate itself impacted by UV light and the yellow UV luminescence of the assays. With these premises, the strategy for automatically recognize wells and extract features from images is developed as summarized in the following main steps.

2.8.1. Pre-identification of wells

A good quality and non-distorted image has been manually chosen as a reference. In particular, a crop of the whole well plate is considered and the layers of colour space of interest are extracted. Then Hough circle detection algorithm (Yuen et al., 1990) is applied to extract the positions of the well circles in the well plate image. Circle detection gave quite good results in identifying the wells correctly, but, due to the parameter tweaking and the different prospects of the photos, some issues arise: a semi-automatic procedure is then designed in such a way, by modifying the Hough algorithm parameters iteratively, it stops when the number of circles identified is 96, and their positions overlap the wells on the image. Then, the centre positions and radius values are trimmed according to a virtual grid calculated from the mean of distances between the circle's positions. In this way, a mask for the wells is obtained from the reference image.

2.8.2. Keypoints Extraction

Keypoints Extraction. Our framework uses the SIFT algorithm proposed by Lowe (2004), which identifies and describes key points. In particular, for this stage, the edge of the plate is considered. Each key point has an associated descriptor, invariant to affine transformation or distortion. SIFT generates a set of elements (p, s, r, f), point-descriptors, where p = (x, y) is the location of the key point pixel on the image, s the scale, r the orientation, and f a 128-dim vector generated from local image gradients. Then key points of the reference image and key points of the image are matched according to the best distance ratio.

2.8.3. Homography with RANSAC

Since the matching may not ensure straightforward correspondences, we adopted a robust homography algorithm. In particular, to manage outlier rejection, the homography is calculated with RANSAC (RANdom SAmple Consensus) (Fischler and Bolles, 1981). RANSAC is a general fitting algorithm that samples the correspondence points, calculates the relative orientations on the sampled data, scores the remaining points, and counts how many inliers or outliers would be concerning those points. This process is repeated, and the model with the highest score is kept.

2.8.4. Extraction of features

Once the homography is found, the mask calculated for the reference image can be applied to the image under consideration: ROIs are identified, and the features of the wells can be extracted. In particular, for each well, we extracted multiple features, the mean and truncated mean at 30%, standard deviation, skewness, and entropy for each channel colour, consisting in gray, RGB, LAB, and HSV. Moreover, image EXIF (EXchangeable Image file Format) datatag has also been added to the features. At the end of the feature extraction procedure, we obtained more than 50 features for each well of the well plates.

To better understand how data distributes with respect the extracted features, a 2D PCA analysis has been conducted in the case of fixed UV light (Fig. S1a - Fig. S1b) and in the case of portable UV lamp (Fig. S1c - Fig. S1d). In the first case a good separation of the six classes, representing concentrations, can be observed. Moreover, such separation also emerges for the real values of detected fluorescence. In the PUVc case, a worst class separation is found, also connected to the different number of samples under analysis. However, in this case a similar distribution for real fluorescence values is present. These analyses confirm the fact that extracted features in the pre-processing phase allow to correctly describe the phenomenon under investigation.

Superpositions of points in the PCA plane for the cases of 0 nM- 50 nM–100 nM classes in both sample type considered (UV- PUVc) are mainly attributable to the closeness of fluorescence values: since the features are extracted from images, the PCA analysis confirm that visual differences between the three aforementioned classes are slight, and their description might result similar in the feature space.

2.9. Behind machine learning predictors: The supervised approach

To infer knowledge on the pre-processed data of the multiwell images, machine learning methodologies have been adopted. Since the final desired result was the ability to calculate the fluorescence intensity value and thus the actual concentration of Hg^{2+}, we used random forest (RF), Multi-layer Perceptron (MLP) and XGBoost (XGB) as both classification and regression algorithms. For the first, the classes available in the experiment setting were six (100 μM, 10 μM, 100 nM, 50 nM, 25 nM and 0 nM), and these were used as targets for the selected three methods. Moreover, the obtained outcome attempted also to improve regression by incorporating classification details as new features into the data passed in input to the regression models.

Combining supervised models is a known procedure that is used to make results more robust (Sagi and Rokach, 2018). According to this, in our framework, we used Weighted Average Probabilities as a combining strategy in classification. In the case of regression, instead, the combination of different regressors is returned as the average of expected values. In general, given n categories and m classifiers; the (weighted) majority vote for the classifier is defined by:

$$\hat{y} = arg\ max_i \sum_{j=1}^{m} w_j p_{ij}$$

where p_{ij} is the probability assigned to the i-th category by the j-th classifier. In this way we aggregate, i.e. combine, probabilities to generate one final prediction.

Similar formula is used for regression

$$\hat{r} = \sum_{j=1}^{m} w_j r_j$$

where r_j can be considered the value assigned to the i-th category by the j-th classifier. In our case we used $m = 3$ ML models (MLP, RF, and XGB) with $n = 6$ classes for classification, and we fixed $w_j = 1/3$ for all j.

3. Results and discussion

3.1. Production and characterization of the Vmh2-H3w-GFP protein

A new chimera formed by the hydrophobin Vmh2 from *P. ostreatus* and the H3w peptide, able to bind metals and bearing a tryptophan residue as fluorescent reporter, was produced in *P. pastoris*. GFP was also fused as reporter to track the protein production and immobilization. The recombinant protein was secreted into extracellular medium, achieving about 50 mg L^{-1} yield after concentration and dialysis. This chimera (0.1 mg mL^{-1}) was directly used for multiwell plate coatings and then GFP was removed taking advantage of the presence of the thrombin recognition site linking Vmh2-H3w and GFP. Thanks to the adhesive properties of Vmh2, H3w peptide resulted tightly bound to the surface, even after several washes with buffer, as confirmed by fluorescence emission at 360 nm after excitation at 295 nm (Fig. 2a), due to the single tryptophan residue present in the sequence of H3w (Vmh2 does not contain neither tyrosine nor tryptophan residues). Unexpectedly, the fluorescence spectrum showed a high emission in the visible region among 400 and 550 nm (Fig. 2a), confirmed by the fact that a strong greenish fluorescence was visible by the naked eye when the wells containing the immobilized chimera were observed under an UV emitting lamp (Fig. 2c). In recent years many papers have reported that amyloid structures show an intrinsic autofluorescence with an excitation wavelength of 345 nm and an emission at about 450 nm, even if these values can change depending on the amyloidogenic protein (Sirangelo et al., 2018). Very intriguingly the amyloid autofluorescence has been observed also in the case of proteins without aromatic residues (Del Mercato et al., 2007) thus ruling out the possibility that it is an artifact due to the (photo)oxidation of tyrosine and/or tryptophan residues, as suggested by some authors (Fricano et al., 2019). Currently the most plausible explanation – even if not the sole – is that autofluorescence is caused by a partial delocalization of π-electrons of peptide bonds along the extended β-sheet structure typical of amyloid fibrils (Sirangelo et al., 2018). On the basis of these reports, the fluorescence of the Vmh2-H3w chimera and of the native Vmh2 after immobilization was measured by exciting at 345 nm. Both proteins showed the typical amyloid autofluorescence with the expected maximum at 450 nm (Fig, 2a and b), thus confirming that also Vmh2 fibrils are autofluorescent and that this phenomenon cannot be attributed to any chemical modifications of tyrosine or tryptophan residues. Therefore, it can be concluded that the anomalous spectrum of Vmh2-H3w chimera is, likely, the sum of the emissions of tryptophan in H3w (about 360 nm) and amyloid fibrils (about 450 nm). Very interestingly the addition of 1 μM Hg^{2+} to immobilized Vmh2-H3w chimera caused a significant decrease both of the tryptophan fluorescence and of the amyloid fluorescence (Fig. 2a). The next sections show that both the emission in the near UV and in the visible spectrum can be used to develop Hg^{2+} sensing devices.

3.2. Evaluation of metal binding capacity

As expected, the fluorescence emission intensity of the immobilized peptide H3w, recorded at 360 nm, gradually decreased with the increased amounts of copper (II) and zinc (II), beyond Hg^{2+} (Fig. 3a). No variation was measured in the presence of the other metals Ni^{2+}, Co^{2+}, and Mg^{2+}, indicating that they are not bound to the peptide, as already demonstrated by Donadio et al. (2016) and Siepi et al. (2018).

Even if binding of Hg^{2+}, Cu^{2+} and Zn^{2+} to the chimera was expected on the basis of the known metal selectivity of the H3w peptide (Donadio et al., 2016; Siepi et al., 2018), the ability of Zn^{2+} to induce quenching of tryptophan fluorescence was not. The well-known ability of Hg^{2+}, and Cu^{2+} to act as quenchers is due to their redox active nature, on the other hand Zn^{2+}, a redox-inactive metal, usually does not cause fluorescence quenching. Therefore, we speculated that the binding of Zn^{2+} might cause quenching indirectly by inducing a conformational change. In particular, it has been demonstrated that only Zn^{2+} induces the dimerization of the H3w peptide (Donadio et al., 2016; Siepi et al., 2018), an event that could affect tryptophan fluorescence. Considering this hypothesis, we progressively reduced the protein concentration in solution to disfavour possible dimerization events. As hypothesized, when 5 μg ml^{-1} of Vmh2-H3w were used, a negligible decrease of fluorescence intensity at varying Zn^{2+}concentration was observed (Fig. 3b). Moreover, no significant difference in the immobilization yield was measured varying the protein amount (about 85%). Therefore this amount was chosen for further immobilization experiments, verifying that the presence of Zn^{2+} at the various tested concentration did not affect the tryptophan fluorescence.

On the other hand, the response of the system to Hg^{2+} and Cu^{2+} was

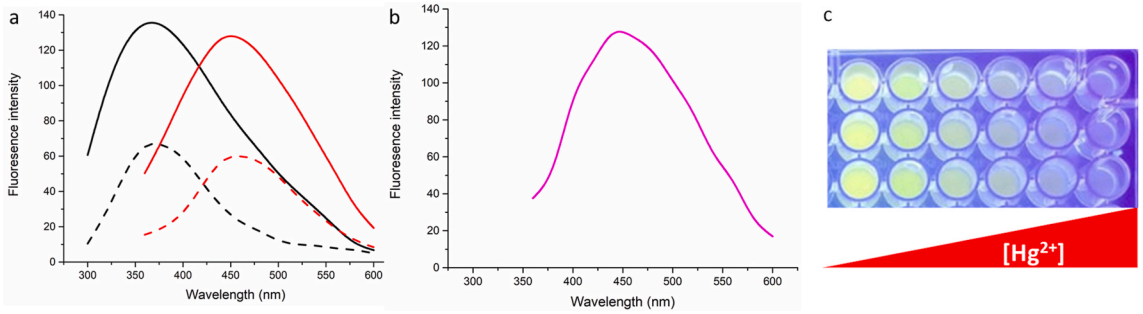

Fig. 2. Fibril autofluorescence. (a) Spectra of fluorescence intensity emission of immobilized Vmh2-H3w at 5 μg mL^{-1} after excitation of Trp at 295 nm (black) and after excitation of fibrils at 445 nm (red) alone (continuous line) and in the presence of 1 μM Hg^{2+} (dashed line). **(b)** Spectra of fluorescence intensity emission of immobilized Vmh2 from *P. ostreatus* at 5 μg mL^{-1} after excitation of fibrils at 445 nm. **(c)** Image of multiwell plate containing the immobilized chimera observed under an UV emitting lamp in the presence of increasing amount of Hg^{2+}. (For interpretation of the references to colour in this figure legend, the reader is referred to the Web version of this article.)

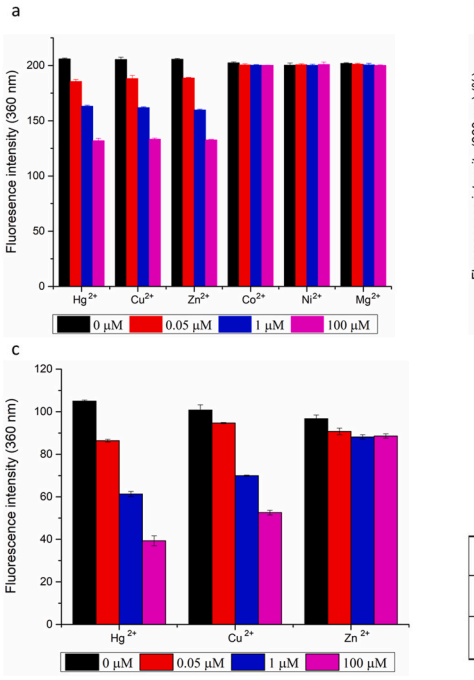

d

	Fluorescence Intensity (360 nm) before ascorbic acid				Fluorescence Intensity (360 nm) after ascorbic acid			
	0	50 nM	1 μM	100 μM	0	50 nM	1 μM	100 μM
Cu^{2+}	101± 1	92± 1	69± 1	51± 1	100± 1	99± 1	97± 1	95± 1
Hg^{2+}	105± 1	84± 1	61± 1	36± 1	105± 1	83± 1	60± 1	36± 1
Cu^{2+}+Hg^{2+}	105± 1	88± 1	63± 1	45± 1	105± 1	83± 1	60± 1	36± 1

Fig. 3. Metal assay. (**a**) Fluorescence intensity emission of immobilized Vmh2-H3w at 360 nm vs the concentration after incubation with different metals. The Vmh2-H3w immobilization was performed at 0.1 mg mL^{-1}. (**b**) Fluorescence intensity emission of Vmh2-H3w at 360 nm at different concentration after incubation with different concentration of Zn^{2+}. (**c**) Fluorescence intensity emission of Vmh2-H3w immobilized at 5 μg mL^{-1}after incubation with different concentration of Hg^{2+}, Cu^{2+} and Zn^{2+}. (**d**) Fluorescence intensity emission at 360 nm of Vmh2-H3w immobilized at 5 μg mL^{-1} incubated with different concentration of Hg^{2+}, and Cu^{2+} before and after treatment with ascorbic acid. Results of two technical replicates of at least three biological replicates were analysed. Standard deviations among replicates were less than 5%.

similar even at the lowest protein amount, (Fig. 3c). In order to selectively bind Hg^{2+}, Cu^{2+} was reduced to Cu^{1+} with 100 μM ascorbic acid, in the hypothesis that Cu^{1+} should bind to the histidine rich motif with considerably lower affinity than Cu^{2+} (Fig. 3d). As it is possible to see from the reported data, reduction with ascorbic acid prevented copper binding, while it did not change the response of the system to Hg^{2+}, thus rendering the system capable to selectively detect Hg^{2+} in the sample.

The ability of the immobilized peptide to bind Hg^{2+}, Cu^{2+} and Zn^{2+} was confirmed by mass spectrometry analysis, measuring the concentration of the different metals before and after the incubation with the immobilized peptide (Table S1). Actually, both Hg^{2+} and Cu^{2+} were barely detectable after incubation, unless the ascorbic acid treatment hindered copper binding. As far as Zn^{2+} is concerned, the less was Hg^{2+} concentration, the higher Zn^{2+} was bound, although no fluorescence variation was registered.

3.3. Development of an optical biosensor

Vmh2-H3w immobilized into a multiwell plate was used to develop a fast and easy to use optical biosensing platform able to respond to Hg^{2+}concentration by decreasing fluorescent intensity emission. A good logarithmic relationship between the fluorescence intensity at 360 nm and the metal concentration was obtained (Fig. 4a) and the results are also reported in a logarithmic scale in order to highlight that fluorescence changed in a range of several orders of magnitude (Fig. 4b). The relationship between the Vmh2-H3w fluorescence and the Hg^{2+} concentration was analysed by fitting the data using the equation (Eq. (1)):

$$y = a + b\ log(x) \quad (1)$$

The correlation with experimental results of the model was assessed by the value determined by the best fitting procedure (Fig. S2, Fig. S2, Table S2), indeed, the measured blank is compatible with the blank of the best fitting.

To assess the potential of H3w as a probe for Hg^{2+}, the detection limit (LOD), determined according to Hao and coworker (2018), was 0.4 nM. The same LOD was also obtained when tap water was used as matrix (Fig. S2c, Fig. S2d, Table S2), a value lower than the maximum permissible level of Hg^{2+} (1.00×10^{-8} M) in drinking water.

Since a major challenge for Hg^{2+} detection is its quantification in seawater, we verified the ability of the immobilized peptide to bind

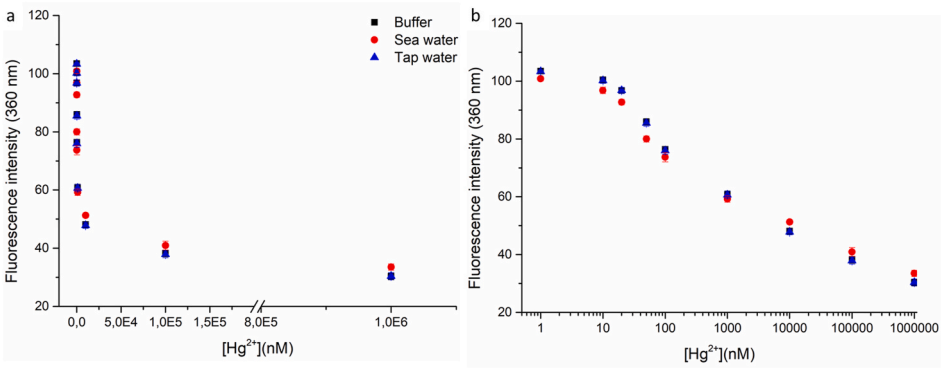

Fig. 4. Biosensing platform evaluation. (a) Calibration curve of Hg^{2+} concentration vs fluorescence intensity at 360 nm in buffer (black square), tap water (blue triangle) and in sea water (red circle). **(b)** Logarithmic plot of the calibration curve of Hg^{2+} concentration vs fluorescence intensity at 360 nm in in buffer (black square), tap water (blue triangle) and in sea water (red circle).

Hg^{2+} in this matrix. Indeed, a set of experiments was performed in the presence of marine water collected at Paestum (Salerno, Italy). The fluorescence intensity was slightly affected by seawater (Fig. 4), and the calculate LOD (0.3 nM) was very close to that obtained in buffer (Fig. S2e, Fig. S2f, Table S2), also considering the natural concentration of this metal in marine water picomolar range (Mills, 2012; Cossa et al., 2009). The sensitivity of the herein developed biosensor is of the same order of magnitude of those based on different measurement methods (Ding et al., 2015; Zhang et al., 2016; Li et al., 2019; Sadani et al., 2019). On the other hand, the development of more sensitive biosensors was only obtained through the exploitation of advanced nanomaterials, such as metal nanoparticle, carbon materials, hybrid materials, and quantum dots (Liu et al., 2019).

The stability and reusability of the immobilized protein is another important characteristic of this kind of biodevices. Therefore, the stability was evaluated by measuring the fluorescence intensity of the Vmh2-H3w chimera during the time. The fluorescence intensity was measured every day in different wells of a plate stored dry at room temperature. No significant variation of the fluorescence intensity of the immobilized peptide was observed at least after 40 days at room temperature (Fig. S3).

In order to test the reusability of the sensor, the multiwell was treated with a chelating agent. Two hours incubation with 10 mM EDTA allowed removal of the metal-bound to the peptide and reuse of the functionalized multiwell up to three times (Fig. S3).

3.4. The coupled learning strategy

Since the fibril autofluorescence can be exploited to detect the presence of heavy metals also emitting different intensities of visible light, such phenomenon can be used to acquire through a camera a digital image. This acquired data collects information about the fluorescence of samples containing different concentrations of heavy metals; thus, it can be analysed with image processing techniques and Machine Learning tools.

The supervised models were trained by splitting the wells' dataset into a train, and test sets randomly picked, with an 80–20 proportion. The results have been validated with the overall accuracy for the classification task and with Mean Absolute Error (MAE) and Root Mean Squared Error (RMSE) for the regression part.

The feature extraction was run once for each experimental setting by fixing the correct reference image and colour channel to extract feature key points and descriptors for matching. Afterwards, for each light setting, the supervised learning procedure was run 15 times, 5 times for each of the available techniques (classification, regression, and regression with classification features) to obtain the average and the standard deviation values of the evaluation metrics.

Regarding the classification task, (Table S3), the best accuracy, which is close to 95% for UVc data and to 85% for PUVc data, is obtained by the combined model in both light settings.

It is worth noticing that the accuracy results much higher in stationary UV light, probably due to the higher quality of photo acquisition (very little inclination, more homogeneous light conditions) procedure. Moreover, the data related to portable UV acquisition are quite sensitive to light reflections, and wells fluorescence tends to be less related to the concentration. Nevertheless, the accuracy predicted is quite reassuring: the high values obtained confirm the approach's effectiveness.

For regression, performances have been evaluated by calculating the MAE and the RMSE. . Within the same light settings, the combined methodology performs better or is the second-best solution concerning other approaches, presenting MAE and RMSE error measures of 1.8 ± 0.2 and 3.0 ± 0.1 (5.0 ± 0.2 and 7.4 ± 0.4) in the case of pure regression, and of 1.0 ± 0.1 and 2.7 ± 0.3 (4.0 ± 0.4 and 7.5 ± 0.7) in the case of class-regression for UVc (PUVc) data. Moreover, it is worth underlining that the strategy of considering the outcomes of the classification model as features for the regression problem, far enhance the quality of the prediction in terms of MAE.

In general, among the experimental settings, also in this case, the best results are obtained in the case of stationary UV lighting.

In order to assess the performances of the proposed prediction strategies, results obtained by the combined method have also been compared with ones achieved by widely used methods in literature, namely SVM for classification and PLS for regression.

SVM is a well known classification algorithm whose objective is to build separation hyperplanes that, partitioning the feature space, allow to classify the samples according to their position with respect to them.

As regards the regression, the PLS method builds a linear regression model between features and targets in a projected space, looking for the direction in the space of the firsts that explains the maximum variance direction in the space of the seconds.

Our predictive methodology always outperform SVM and PLS (Table S3), confirming the reliability and effectiveness of the approach.

Finally, since the feature extraction process generates a high number of variables, an investigation on their impact on both the classification and the regression problems becomes necessary. Exploiting the characteristics of tree-based algorithms, which provide feature importance scores based on the reduction in the criterion used to select split points, the contribution of the generated variables on the predictive tasks has been analysed.

Single feature scores, and their cumulative importance, have been analysed (Fig. S4) in the case of classification and regression for both the UV and PUVc data. It has been observed that the importance scores span in a very narrow interval in all the cases, and their cumulative sum exhibit a slow growth since such scores turn out to be quite evenly distributed. What emerges is that most of the features contribute to the description of the data, and noisy components cannot be easily

identified and isolated. These considerations are also confirmed by the prediction outcomes, with and without a selection of features based on a threshold on the cumulative importance score (Table S4) for the case of UVc data (Table S5) and for the case of PUVc data: even if the number of considered features is reduced by 25% circa in the case a threshold of 0.95 is set, no significant variations in performances can be encountered. On one hand this highlights a number of highly correlated features, whose impact on the predictive abilities of the models is neglectable. On the other hand, excluding these features does not improve classification performances, meaning that no noise reduction in the data is obtained. This last consideration is also confirmed by the fact that further reductions of the threshold cause a degradation of model performances, which means that predictive variables start to be excluded.

The behaviour described so far can be also found in predictions related to the regression task: the model exhibits a MAE of 2.2 ± 0.3, 4.7 ± 0.4 and a RMSE of 3.7 ± 0.2, 7.9 ± 0.3 in the cases of UVc and PUVc data, respectively. Moreover, in this case a slight worsening of the performances can be observed. This confirms the generality of what has been observed in the specific context of classification discussed above, and motivates the choice of excluding the feature selection step from the proposed pipeline.

3.5. Analytical performance for detection of Hg^{2+}

In order to verify that the developed method allows the correct determination of Hg^{2+}, recovery studies were conducted by spiking 50 nM and 100 μM of Hg^{2+} in the samples and calculating the concentration with the herein developed methods (Table 1). The results obtained confirmed the reliability of both developed biosensor systems.

4. Conclusions

In this paper an effective and efficient biosensing platform for Hg^{2+} quantification in sea water was developed based on the new chimera Vmh2-H3w. The biosensor developed herein has the advantage of an easy and effective immobilization procedure, the possibility of measuring the Hg^{2+} concentration in water directly, and the chance of simultaneous analysis by non-qualified personnel. Hg^{2+} is specifically recognized also in the presence of other metals, and its concentration is detected starting from to 0.4 nM in tap water and 0.3 nM in sea water. Moreover, a coupled framework which exploits the visible fluorescence of the fibril and the predictive abilities of different Machine Learning models has been designed to classify and predict the fluorescence intensity values related to the concentration of heavy metals acquired with a cheap acquisition hardware of a smartphone.

Future studies will include improving the overall classification accuracy and reducing regression errors using various light settings, camera devices, and other types of well plates. Finally, a calibration curve should be determined for the final user.

CRediT authorship contribution statement

Anna Pennacchio: Investigation, Methodology, Validation, Formal analysis, Writing – original draft. **Fabio Giampaolo:** Investigation, Methodology, Validation, Formal analysis, Writing – original draft. **Francesco Piccialli:** Conceptualization, Validation, Supervision, Writing – review & editing. **Salvatore Cuomo:** Conceptualization, Validation, Supervision, Writing – review & editing. **Eugenio Notomista:** Conceptualization, Validation, Supervision, Writing – review & editing. **Alessandra Piscitelli:** Conceptualization, Validation, Supervision, Project administration, Writing – review & editing. **Paola Giardina:** Conceptualization, Validation, Supervision, Project administration, Writing – review & editing.

Table 1
Recovery studies of the developed sensor.

Spiked concentration Hg^{2+} (μM)	Measured concentration Hg^{2+} (μM)		Recovery (%)	
	Optical detection	Trained system (UVc)	Optical detection	Trained system (UVc)
0.05	0.06	0.05	120	100
100	105	100	105	100

Declaration of competing interest

The authors declare that they have no known competing financial interests or personal relationships that could have appeared to influence the work reported in this paper.

Acknowledgments

This project is funded by the Italian Education, University and Research Ministry (MIUR) and co-funded by European Union's Horizon 2020 research and innovation program under the framework of ERA-NET Cofund MarTERA (Maritime and Marine Technologies for a new Era), FLAshMoB, Functional Amyloid chimera for Marine Biosensing (ID: 172). This work was also supported by grants from the University of Naples Federico II, Italy (000023_ALTRI_CDA_75_2021_-FRA_PISCITELLI) "Intelligent biosensors based on chimeric proteins (BIOCHIP)"

Appendix A. Supplementary data

Supplementary data to this article can be found online at https://doi.org/10.1016/j.bios.2021.113696.

References

Ali, H., Khan, E., Sajad, M.A., 2013. Chemosphere 91 (7), 869–881.
Akmal Munir, R., Santoso, J., 2019. 5th International Conference on Science in Information Technology (ICSITech) 176–181. https://doi.org/10.1109/ICSITech46713.2019.8987480.
Berg, B., Cortazar, B., Tseng, D., Ozkan, H., Feng, S., Wei, Q., Chan, R.Y.-L., Burbano, J., Farooqui, Q., Lewinski, M., Di Carlo, D., Garner, O.B., Ozcan, A., 2015. ACS Nano 9, 7857–7866. https://doi.org/10.1021/acsnano.5b03203.
Canny, J., 1986. IEEE Trans. Pattern Anal. Mach. Intell. 8, 679–698. https://doi.org/10.1109/TPAMI.1986.4767851.
Choi, O., Kim, B., An, J., Min, K., Kim, Y.H., Um, Y., Oh, M., Sang, B., 2011. Enzym. Microb. Technol. 49, 441–445.
Chopra, A.K., Pathak, C., Prasad, G., 2009. J. Appl. Nat. Sci 1 (1), 99–108.
Cossa, D., Averty, B., Pirrone, N., 2009. Limnol. Oceanogr. 54 (3), 837–844.
Cui, F., Yue, Y., Zhang, Y., Zhang, Z., Zhou, H.S., 2020. ACS Sens. 5, 3346–3364. https://doi.org/10.1021/acssensors.0c01424.
de la Calle, I., Páez-Cabaleiro, J., Lavilla, I., Bendicho, C., 2019. Talanta 199, 449–456.
Del Mercato, L.L., Pompa, P.P., Maruccio, G., Della Torre, A., Sabella, S., Tamburro, A. M., Cingolani, R., Rinaldi, R., 2007. Proc. Natl. Acad. Sci. U. S. A. 104 (46), 18019–18024. https://doi.org/10.1073/pnas.0702843104.
De Silva, T.M., Veglia, G., Porcelli, F., Prantner, A.M., Opella, S.J., 2002. Biopolymers 64, 189–197.
De Stefano, L., Rea, I., De Tommasi, E., Rendina, I., Rotiroti, L., Giocondo, M., Longobardi, S., Armenante, A., Giardina, P., 2009. Eur. Phys. J. E Soft Matter 30 (2), 181–185. https://doi.org/10.1140/epje/i2009-10481.
Ding, J., Li, H., Wang, C., Yang, J., Xie, Y., Peng, Q., Li, Q., Li, Z., 2015. ACS Appl. Mater. Interfaces 7, 11369–11376.
Donadio, G., Di Martino, R., Oliva, R., Petraccone, L., Del Vecchio, P., Di Luccia, B., 2016. J. Mater. Chem. B 4, 6979–6988.
Faccio, G., 2018. Sensors 18, 1204. https://doi.org/10.3390/s18041204.
Fischler, M.A., Bolles, R.C., 1981. Commun. ACM 24, 381–395. https://doi.org/10.1145/358669.358692.
Fricano, A., Librizzi, F., Rao, E., Alfano, C., Vetri, V., 2019. Biochim. Biophys. Acta Protein Proteonomics 1867 (11). https://doi.org/10.1016/j.bbapap.2019.07.011, 140258. 140258.
Gravagnuolo, A.M., Morales-Narváez, E., Longobardi, S., Da Silva, E.T., Giardina, P., Merkoçi, A., 2015. Adv. Funct. Mater. 25, 2771–2779.
Gu, L., Zheng, T., Xu, Z., Song, Y., Li, H., Xia, S., Shen, L., 2019. Spectrochim. Acta A Mol. Biomol. Spectrosc. 207, 88–95.
Hao, P.V., Xuan, C.T., Thanh, P.D., Thuat, N.T., Hai, N.H., Tuan, M.A., 2018. J Sci-ADV Mater Dev 3 (2), 129–138.

Hatiboruah, D., Das, T., Chamuah, N., Rabha, D., Talukdar, B., Bora, U., Ahamad, K.U., Nath, P., 2020. Meas. Tech. 154, 107507 https://doi.org/10.1016/j.measurement.2020.107507.
Hennig, S., Rödel, G., Ostermann, K., 2016. Sensors 16, 602.
Huang, L., Zhu, Q., Zhu, J., Luo, L., Pu, S., Zhang, W., Zhu, W., Sun, J., Wang, J., 2019. Inorg. Chem. 58 (2), 1638–1646.
James, G., Witten, D., Hastie, T., Tibshirani, R., 2013. An Introduction to Statistical Learning 112. Springer.
Justino, C.I.L., Duarte, A.C., Rocha-Santos, T.A.P., 2017. Sensors 17, 2918. https://doi.org/10.3390/s17122918.
Jyothi, N.R., Abdulkhader, N., Farook, M., 2020. Intech. https://doi.org/10.5772/intechopen.90333.
Kabir, K.M.M., Jampaiah, D., Kandjani, A.E., Mullett, M., Tardio, J., Sabri, Y.M., Bhargava, S.K., 2019. Sensor. Actuator. B Chem. 290, 453–458.
Kaur, J., Vergara, A., Rossi, M., Gravagnuolo, A.M., Valadan, M., Corrado, F., Contei, M., Gesuele, F., Giardina, P., Altucci, C., 2017. RSC Adv. 7, 50166. https://doi.org/10.1039/c7ra09878b.
Kim, H., Choi, S.K., Ahn, J., Yu, H., Min, K., Hong, C., Shin, I.S., Lee, S., Lee, H., Im, H., Ko, J., Kim, E., 2021. Sensor. Actuator. B Chem. 329, 129248 https://doi.org/10.1016/j.snb.2020.129248.
Koji, T., Kazutaka, N., Yumehiro, H., Tomoki, N., Yasuo, A., Akio, K., 2006. Biotechnol. Bioeng. 96, 1023–1029.
Li, J., He, Q., Wu, L., Sun, J., Zheng, F., Li, L., Liu, W., Liu, J., 2019. Microchem. J. 153, 104459.
Liu, T., Chu, Z., Jin, W., 2019. J. Mater. Chem. B 7, 3620.
Lowe, D.G., 2004. Int. J. Comput. Vis. 60, 91–110. https://doi.org/10.1023/B:VISI.0000029664.99615.94.
Mahurpawar, M., 2015. Int. J. Res -Granthaalayah 3 (9), 1–7. https://doi.org/10.29121/granthaalayah.v3.i9SE.2015.3282.
Mills, G., 2012. Sens. Rev. 32 (1), 17–28.
Nour, H.E., El-Sorogy, A.S., 2020. Environ. Earth Sci. 79, 274.
Pennacchio, A., Cicatiello, P., Notomista, E., Giardina, P., Piscitelli, A., 2018. Biol. Chem. 399 (8).
Piscitelli, A., Pennacchio, A., Longobardi, S., Velotta, R., Giardina, P., 2017a. Biotechnol. Bioeng. 114, 46–52. https://doi.org/10.1002/bit.26049.
Piscitelli, A., Pennacchio, A., Cicatiello, P., Politi, J., De Stefano, L., 2017b. Biosens. Bioelectron. 87, 816–822.
Puopolo, R., Sorrentino, I., Gallo, G., Piscitelli, A., Giardina, P., Le Goff, A., Fiorentino, G., 2021. Sci. Rep. 11, 2991.
Sadani, K., Naga, P., Mukherjia, S., 2019. Biosens. Bioelectron. 134, 90–96.
Sagi, O., Rokach, L., 2018. J. Adv. Res. 8, e1249. https://doi.org/10.1002/widm.1249.
Saleh, T.A., Fadillah, G., Ciptawati, E., Khaled, M., 2020. TrAC Trends Anal. Chem. (Reference Ed.) 132, 116016.
Shah, A., Nisar, A., Khan, K., Nisar, J., Niaz, A., Ashiq, M.N., Akhter, M.S., 2019. Electrochim. Acta 321, 134658.
Siepi, M., Oliva, R., Petraccone, L., Del Vecchio, P., Ricca, E., Isticato, R., Lanzilli, M., Maglio, O., Lombardi, A., Leone, L., Notomista, E., Donadio, G., 2018. PLoS One 13 (10), e0204164. https://doi.org/10.1371/journal.pone.0204164.
Sirangelo, I., Borriello, M., Irace, G., Iannuzzi, C., 2018. Biophys 5 (2), 155–165. https://doi.org/10.3934/biophy.2018.2.155.
Sorrentino, I., Giardina, P., Piscitelli, A., 2019. Appl. Microbiol. Biotechnol. 103, 3061–3071.
Sorrentino, I., Gargano, M., Ricciardelli, A., Parrilli, E., Buonocore, C., de Pascale, D., Giardina, P., Piscitelli, A., 2020. Int. J. Biol. Macromol. 164, 2293–2300.
Vardhan, K.H., Kumar, P.S., Panda, R.C., 2019. J. Mol. Liq. 290, 111197.
Vashist, S.K., Luong, J.H.T., 2019. Point-of-Care Technologies enabling next-generation healthcare monitoring and management. Biomed. Eng. 27–79. https://doi.org/10.1007/978-3-030-11416-9_2.
Yuen, H., Princen, J., Illingworth, J., Kittler, J., 1990. Image Vis Comput. 8, 71–77. https://doi.org/10.1016/0262-8856(90)90059-E.
Zhang, B., Ma, P., Gao, D., Wang, X., Sun, Y., Song, D., Li, X., 2016. Spectrochim. Acta A Mol. Biomol. Spectrosc. 165, 99–105.